Bioresource Technology 460 (2026) 135390

Contents lists available at ScienceDirect

Bioresource Technology

journal homepage: www.elsevier.com/locate/biortech

Impact of emerging contaminants on phosphorus recovery in batch and fluidized-bed reactors: Kinetic and mechanistic insights

Xianfei Wang [a,1], Degui Gao [b,1], Mengyu Ma [a,1], Ruxin Han [a], Bing Li [b], Dawei Li [a], Feihu Li [a,c,*]

[a] Aquatic Chemistry & Ecomaterials Laboratory (ACE Lab), School of Environmental Science and Engineering, Nanjing University of Information Science and Technology, 219 Ningliu Road, Nanjing 210044, China
[b] Water Research Center, Tsinghua Shenzhen International Graduate School, Tsinghua 518055, Shenzhen, China
[c] NUIST Reading Academy, Nanjing University of Information Science and Technology, 219 Ningliu Road, Nanjing 210044, China

HIGHLIGHTS

- EC impacts on struvite formation kinetics and purity were evaluated in BRs and FBRs.
- HA and Cu + TC inhibit crystallization by surface-mediated interactions and Mg^{2+} complexation.
- Fluidized bed hydraulics mitigate kinetic inhibition and enhance pellet growth.
- DFT reveals EC–Mg^{2+} interactions are dominated by weak ion–dipole forces.
- Ternary complexes bridged by Mg^{2+}/Cu^{2+} are the most stable species in matrices.

GRAPHICAL ABSTRACT

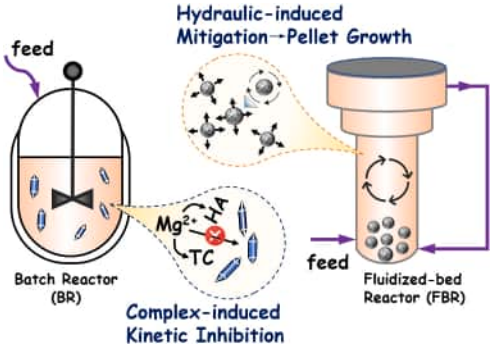

ARTICLE INFO

Keywords:
Struvite crystallization
Swine wastewater
Copper-tetracycline complex
DFT calculation
IRI analysis

ABSTRACT

Struvite crystallization is a sustainable strategy for phosphorus (P) recovery, yet the presence of emerging contaminants (ECs) poses significant obstacles by disrupting struvite crystallization kinetics and compromising product purity and thus its potential agronomic safety. This study systematically investigates the impacts of tetracycline (TC), polyethylene terephthalate (PET), Cu^{2+}, and humic acid (HA) on struvite formation using both batch reactors (BRs) and fluidized-bed reactors (FBRs). Batch experiments revealed that HA and Cu+TC act as potent inhibitors through a combination of surface-mediated interactions and Mg^{2+} complexation, reducing the apparent crystallization rate of struvite. Conversely, FBR results demonstrated that specific hydraulic conditions can mitigate the kinetic inhibition of Cu+TC, yielding larger pellets (~ 1342 vs ~ 1138 μm in diameter) with apparent Cu^{2+} incorporation into the pellet matrix. Trials with real swine wastewater verified that excessive dissolved organic matter and Ca^{2+} favor the formation of amorphous phases rather than crystalline struvite (84.9% vs 2.7% in the amorphous fraction). Density functional theory calculations indicated that the Mg^{2+} complexation is primarily governed by non-covalent ion–dipole (Mg–O) interactions between HA/TC with Mg^{2+}.

* Corresponding author at: Aquatic Chemistry & Ecomaterials Laboratory (ACE Lab), School of Environmental Science and Engineering, Nanjing University of Information Science and Technology, 219 Ningliu Road, Nanjing 210044, China.
E-mail address: fhli@nuist.edu.cn (F. Li).
[1] These authors contributed equally.

https://doi.org/10.1016/j.biortech.2026.135390
Received 23 April 2026; Received in revised form 9 July 2026; Accepted 12 July 2026
Available online 13 July 2026

Besides, ternary complexes bridged by metal-O were identified as the most stable species (HA–Cu/Mg–TC) within these matrices, which may enhance the mobility or persistence of such ECs in aquatic environments. Consequently, robust P recovery requires integrated strategies—combining pre-treatment to remove strong inhibitors with specific FBR conditions (hydraulics and extended retention time) that leverage crystal growth and conglomeration. This work provides the kinetic and mechanistic insights necessary for developing such integrated solutions, advancing our understanding of EC-mediated crystallization of struvite and the viability of P recovery from increasingly complex waste streams.

1. Introduction

Phosphorus (P) is a non-renewable, geologically scarce element fundamental to global food security, underpinning all agricultural systems through fertilizer production (Desmidt et al., 2015). Its extraction from finite phosphate rock reserves presents a critical supply risk amidst ever-growing demand. Concurrently, the linear economy of phosphorus, viz., from mine to field to water, leads to severe environmental degradation, with excess discharges catalyzing widespread eutrophication, algal blooms, and aquatic ecosystem collapse (Cordell et al., 2009; Jin et al., 2024). This dual dilemma of resource scarcity and pollution necessitates an urgent transition towards a circular phosphorus economy. To this end, recovering phosphorus from anthropogenic waste streams is central to closing the phosphorus loop (Jupp et al., 2021). Wastewater, and particularly nutrient-rich streams like swine effluent and livestock manure, represent significant secondary phosphorus reservoirs (Yang et al., 2025), with concentrations often exceeding 100 mg L^{-1} (Le Corre et al., 2009). Valorizing these "waste" resources offers a compelling environmental imperative—mitigating nutrient pollution at its source—and an economic driver, creating a localized fertilizer supply chain independent of mined phosphate. Struvite ($MgNH_4PO_4{\cdot}6H_2O$) crystallization has emerged as a leading platform technology for such nutrient recovery (Doyle and Parsons, 2002; Kataki et al., 2016; Li et al., 2019). It provides the dual benefit of simultaneously removing phosphorus and ammonia to prevent scaling in treatment infrastructure (e.g., pipelines and anaerobic digesters), while producing a valuable, slow-release fertilizer (Desmidt et al., 2015; Le Corre et al., 2009).

While struvite crystallization for phosphorus recovery is operatively defined by parameters like pH and supersaturation (Mehta and Batstone, 2013), its translation from idealized systems (laboratory scale) to real-world application is challenged by the pervasive complexity of real wastewaters (Yan et al., 2024). The process efficiency and the characteristics of the reclaimed product are notably sensitive to foreign ions and molecular impurities, which are inevitable in waste streams such as swine wastewater (Do et al., 2023; Shih et al., 2017). Aside from the nutrient ions (Mg^{2+}, NH_4^+, PO_4^{3-}), these matrices are laden with a spectrum of emerging contaminants (ECs)—including microplastics (MPs), antibiotics (e.g., tetracycline, TC), heavy metals (e.g., Cu, Zn), and refractory organics—released through anthropogenic activities (Chan et al., 2022; Lou et al., 2018; Ma et al., 2024). For instance, the abundance of MPs in manure from livestock farms ranges from 74 to 1.29 × 10^3 particles kg^{-1} (Wu et al., 2021), most of which are gradually transferred to livestock wastewater, being enriched in nutrient-rich waste streams. Crucially, in a complex matrix like swine wastewater, these ECs enact discrete chemical and physical roles: for instance, polyethylene terephthalate (PET) MPs provide a functionalized solid interface for binding and spreading other pollutants (vectors) (Wang et al., 2020b), tetracycline complexes with cations (Wang et al., 2021), copper (Cu^{2+}) directly competes with Mg^{2+}, and humic acid (HA) acts as a solubilizing polyelectrolyte (Ma et al., 2024; Yan et al., 2024). Their integrated effects can alter nucleation kinetics, crystal growth, and purity of the reclaimed product in either batch (BRs) or continuous fluidized-bed reactors (FBRs) (Yan et al., 2024; Yang et al., 2025; Zahid et al., 2025). Understanding their individual and combined impacts is therefore essential for predicting process performance in authentic nutrient recovery scenarios (Liao et al., 2025; Yang et al., 2025). Moreover, whether conducted in a BR or an FBR, the hydrodynamics and residence timescales inherent to each system can either mitigate or exacerbate such contaminant impacts, posing additional challenges for contaminated feeds (Yan et al., 2024).

Extensive research has established that the presence of competitive ions and organic matter can drastically alter the kinetic pathways of struvite formation. For instance, the inhibitory or altering effects of competing cations, such as Ca^{2+}, which can compete with Mg^{2+}, promoting calcium phosphates and thereby inhibiting struvite nucleation, growth, crystal size, and purity, are well-documented (Chen et al., 2026; Liu and Wang, 2019; Yan and Shih, 2016). Similarly, heavy metals like Cu^{2+} and Cd^{2+} are known to inhibit growth by competing for lattice sites or inducing isomorphous substitution, thus reducing crystal purity and altering morphology (Chen et al., 2023; Perwitasari et al., 2018). Beyond ions, dissolved organic matter (DOM) and specific antibiotics are known to hinder crystal growth through complexation, surface adsorption, steric hindrance, and stabilization of amorphous phases (Yan et al., 2024; Zhang et al., 2016). Notably, the propagation of antibiotic resistance genes (ARGs) within recovered struvite has also raised concerns about product safety (Gao et al., 2024a; Hu et al., 2022; Liao et al., 2025). Despite these insights, a significant knowledge gap persists regarding the multicomponent interference of a complex, realistic contaminant suite—specifically encompassing the above ECs (e.g., PET, TC, Cu^{2+}, etc.) —on both the nucleation and kinetics of crystallization and the final crystal properties (Yan et al., 2024; Zahid et al., 2025). Current literature often treats these ECs in isolation, failing to account for the complex hetero-aggregation and competitive adsorption that occur in poly-contaminated matrices (Chen et al., 2023; Gao et al., 2024b). Furthermore, there is a profound lack of mechanistic depth in existing studies; many existing studies remain empirical, correlating the presence of a contaminant with a change in recovery efficiency or crystal morphology without unraveling the dynamic interference mechanisms occurring at the solid–liquid interface during the early stages of crystallization (Le Corre et al., 2005; Rabinovich and Rouff, 2023). This mechanistic ambiguity hinders the predictive design and the development of robust phosphorus recovery systems facing complex waste matrices.

To this end, this study aims to elucidate the kinetic and mechanistic impacts of a representative ensemble of ECs—PET, TC, Cu^{2+}, and HA—on struvite crystallization and its quality. We employ a coupled experimental strategy designed to bridge fundamental crystallization kinetics with process engineering. This is achieved through a comparative investigation utilizing both the idealized BR and a continuous FBR. The batch experiments are designed to extract apparent kinetic parameters (e.g., apparent crystallization rate constants), allowing for a comprehensive analysis of how these ECs modify the crystal growth indirectly from a kinetic perspective. In parallel, FBR experiments will assess these effects under process-relevant hydrodynamic conditions. By integrating findings from both regimes, we aim to uncover the specific mechanisms that govern the formation of struvite in the presence of these ubiquitous contaminants and to identify the critical thresholds at which these ECs compromise the viability of phosphorus recovery. The insights gained from this work are intended to provide essential design and operational guidelines for enhancing the resilience and efficiency of phosphorus recovery systems, particularly FBRs, in the presence of pervasive and complex EC matrices.

2. Materials and methods

2.1. Chemicals

All chemicals used for struvite crystallization are of analytical pure grade or above. Potassium dihydrogen phosphate (KH_2PO_4, ≥99.0%), ammonium magnesium phosphate hexahydrate ($MgNH_4PO_4 \cdot 6H_2O$, 98.0%), magnesium chloride hexahydrate ($MgCl_2 \cdot 6H_2O$, ≥98.0%), copper chloride dihydrate ($CuCl_2 \cdot 2H_2O$, ≥99.0%), sodium hydroxide (NaOH, ≥99.0%), ascorbic acid (AA), and nitric acid (HNO_3) were purchased from Sinopharm Chemical Reagent Co., Ltd. (Shanghai, China). Humic acid (HA) and tetracycline hydrochloride (TC) were obtained from Aladdin Biochemical Technology Co., Ltd. (Shanghai, China). Ammonium chloride (NH_4Cl, ≥99.5%) was supplied by Lingfeng Chemical Reagent Co., Ltd. (Shanghai, China). Polyethylene terephthalate (PET) of *ca.* 50 μm in size was obtained from Wangda Plastic Materials Co., Ltd. (Dongguan, China) and artificially aged over 20 days using a heat persulfate oxidation (HPO) method (Ma et al., 2024). Ultrapure deionized (DI) water (18.2 MΩ·cm at 25℃) was used to prepare solutions. Considering that PET can rapidly bind heavy metals in both natural and wastewater systems, and many previous studies have documented the impacts of heavy metals and/or antibiotics on struvite precipitation (Perwitasari et al., 2018; Tang et al., 2019; Yan et al., 2024), the selection of metal/antibiotics-loaded microplastics as impurities is well-established and has great environmental relevance. To this end, copper ions and TC species were preloaded onto the aged PET particles by a set of batch adsorption operations (Ma et al., 2024). The resulting Cu/TC-loaded microplastics (denoted as PET-Cu+TC) were then used as complex impurities in the struvite crystallization experiments, as such complex contaminants are most likely to occur in the actual swine wastewaters, rather than being microplastics or heavy metals and TC that exist alone.

2.2. Crystallization in BRs

Following the same procedure as specified earlier (Yan et al., 2024), batch crystallization experiments were performed at standard atmospheric pressure and temperature (*ca.* 25 °C) in a 1000-mL beaker (Fig. 1 a) within a time scale of 60 min. Briefly, solution **a** was prepared by dissolving a certain amount of KH_2PO_4 into 493 mL of DI water, to which a dilute NaOH solution was added to adjust the pH to 11.0 ± 0.2. Likewise, solution **b** was synthesized by combining equimolar amounts of $MgCl_2$ and 2.5 mmol of NH_4Cl with 7 mL of DI water, which was then quickly poured into the beaker with solution **a** and mixed moderately over a magnetic stirrer (INTLLAB, Shenzhen, China). Since the optimal pH window for struvite formation is 8.0–9.5 (Zahid et al., 2025), the

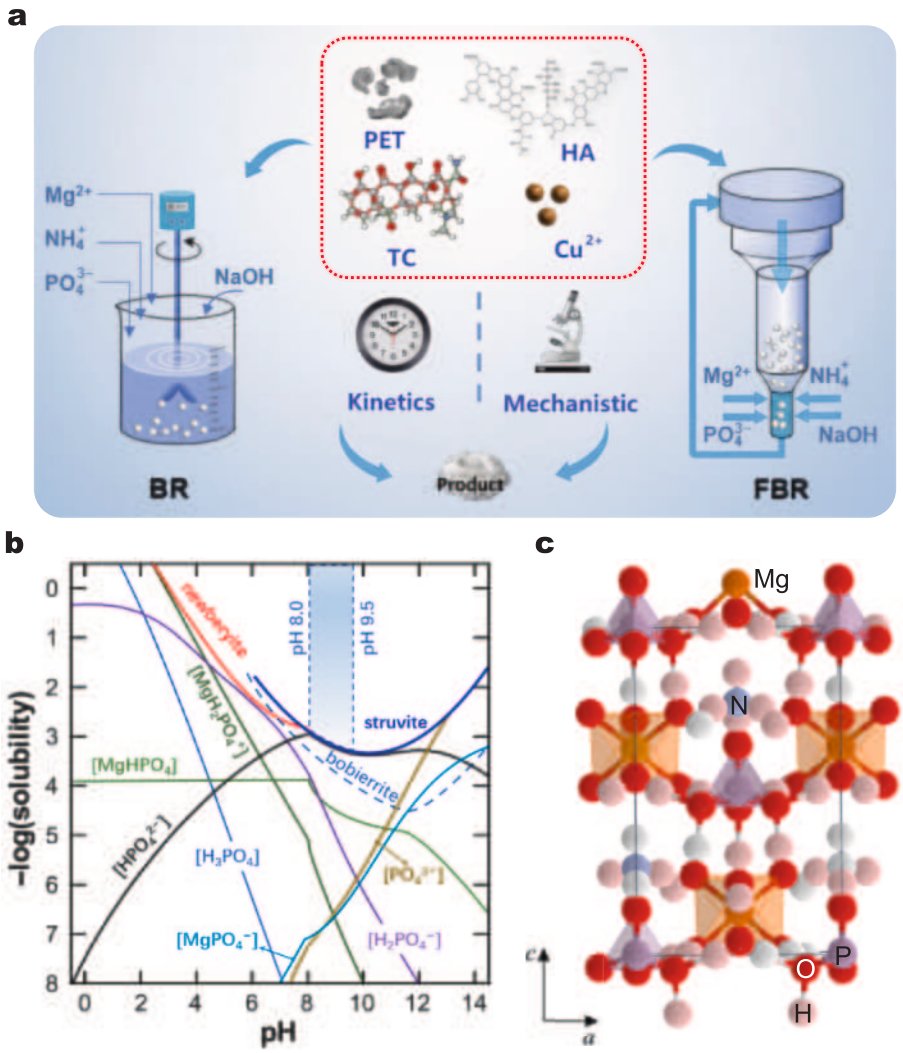

Fig. 1. (**a**) Schematic illumination of struvite crystallization in the presence of typical ECs in batch and fluidized-bed reactors; (**b**) Phase diagram of struvite along with other common phosphates (Note: the pH range of 8.0 – 9.5 studied here is highlighted with a light blue-shaded region), adapted with permission from Shih et al. (2017), Copyright 2017, Elsevier; (**c**) Crystal structure of struvite (Mg, orange; P, light purple; H, light gray; N, light blue; and O, red).

initial pH of the batch reaction matrices was adjusted to 11.0 ± 0.2 to ensure the initial pH of the above mixture being at *ca.* 9.5 (Fig. 1 b). To trace the formation kinetics of struvite crystals (Fig. 1 c), the suspension pH was monitored and recorded every minute using a pH meter (PHS-25, Rex Electric Chemical), while the concentration of remaining soluble phosphate (PO_4^{3-}-P) was measured every 5 min using the ascorbic acid method as described elsewhere (Li et al., 2016). To begin with, the influence of initial phosphorus concentration ($[PO_4]_0$) on the crystallization kinetics of struvite was explored over the range of 20 − 250 mg L^{-1} (i.e., 20, 50, 120, and 250 mg L^{-1}) with a constant Mg:P molar ratio (Mg/P ratio) maintaining at the theoretical stoichiometry of struvite, 1.0. Then, the effect of the Mg/P ratio was evaluated over the range of 0.8 − 1.4 (i.e., 0.8, 1.0, 1.2, and 1.4) at a constant $[PO_4]_0$ of 50 mg L^{-1}. Given that the phosphorus concentration in real swine wastewater typically ranges from 20 to 80 mg L^{-1}, a constant $[PO_4]_0$ of 50 mg L^{-1} and a Mg/P ratio of 1.0 were then chosen for the subsequent experiments unless otherwise stated. HA, copper (Cu^{2+}), and TC were chosen to evaluate the impact of emerging contaminants on the crystallization of struvite. Specifically, the batch crystallization experiments were carried out separately in the presence of HA (2–20 mg L^{-1}) and Cu^{2+} plus TC (Cu+TC, 0.03–0.24 mM) with a constant $[PO_4]_0$ of 50 mg L^{-1} and a Mg/P ratio of 1.0 to explore their impacts on struvite formation.

The crystallization kinetic rate constant was determined by fitting the data of remaining soluble phosphate in the suspensions to a first-order kinetic model that was formulated as follows (Nelson et al., 2003),

$$-\frac{dC}{dt} = k(C_0 - C_e) \quad (1)$$

$$\ln(C - C_e) = -kt + \ln(C_0 - C_e) \quad (2)$$

where $\boldsymbol{k}$ is the rate constant (h^{-1}), $\boldsymbol{C}$ is the soluble phosphate (reactant) concentration (mg L^{-1}) at time $\boldsymbol{t}$, $\boldsymbol{C}_0$ and $\boldsymbol{C}_e$ are the phosphate (PO_4^{3-}-P) concentrations at the initial and equilibrium state (mmol·L^{-1}).

2.3. Crystallization in FBRs

Struvite crystallization experiments were also conducted in a homemade fluidized-bed reactor (FBR), which features an upper section with a diameter of 4 cm and height of 20 cm, and a lower section with a diameter of 2 cm and height of 80 cm (total volume ~ 502 mL, see supplementary material Fig. S1). The feed solution (ca. 5 L) was prepared by dissolving equimolar amounts of KH_2PO_4, $MgCl_2{\cdot}6H_2O$, and NH_4Cl to yield a 6.45 mM synthetic solution. NaOH solution (0.1 M) was used as the alkaline feed to adjust the initial pH of the feed solution up to ~ 11.0 ± 0.2, boosting struvite crystallization in the FBR setup and ensuring the pH of the effluent is above 9.0 during the nucleation and growth period of struvite. To begin with, the feed solution was pumped into the FBR via a peristaltic pump (BT-100, Longer Pump Co., China) at a flow rate of 5 mL min^{-1} for 5 min. Subsequently, the alkaline solution was fed into the FBR setup using another pump at the same rate (5 mL min^{-1}), while the third pump connecting the bottom and the upper part of the FBR setup was launched at 50 mL min^{-1} to circulate the mixture, achieving a complete fluidization of the suspension (recirculation ratio = 500%). These parameters were maintained constant throughout the crystallization experiments. To prevent clogging of the inlet at the column bottom, a certain amount of glass beads (with a diameter of ~ 0.5 cm) was packed into the FBR column to form a 3.5 cm high support layer, ensuring uniform distribution to support the granulation bed. After circulating for 3 days, the crystallization process was terminated, and the struvite precipitates were reclaimed from the FBR bottom. Likewise, the effects of ECs, including PET, Cu^{2+}-TC complex, and Cu+TC-loaded PET, on struvite crystallization in FBRs were also investigated with the individual addition of such impurities at the beginning of each circulating operation. Last but not least, an actual swine wastewater (SWW) from a local pig farm was used to explore the effect of natural DOM and other co-occurring species on struvite formation in FBRs.

2.4. Characterization of the reclaimed precipitates

All the precipitate samples obtained from both the BRs and FBRs were reclaimed by centrifugation, then rinsed twice with DI water, followed by drying overnight in an oven at 80℃ for subsequent analysis and characterization. Following a coding format of 'reactor-impurity', the precipitates from BRs are denoted as BR-blank, BR-HA, and BR-Cu+TC, respectively, while the solids from FBRs are denoted as FBR-blank, FBR-PET, FBR-Cu+TC, and FBR-PET@Cu+TC, respectively.

X-ray diffraction (XRD) analysis was performed on a Smart Lab X-ray diffractometer (Rigaku, Japan) equipped with a Cu-target X-ray tube, operating at a power of 2.2 kW. All the mineral phases were identified by using the MDI Jade software (version 9.0, Materials Data, Inc., USA) with the ICDD® PDF-2 database. The mineral compositions in the reclaimed precipitates were calculated by the whole-pattern fitting (WPF) module embedded in the MDI Jade software. Fourier transform infrared (FTIR) spectra data were collected on a Nicolet iS5 spectrometer (Thermo Fisher Scientific, USA) over the wavelength range of 4000 – 400 cm^{-1} using the KBr pellet method. Scanning electron microscopy (SEM) was performed using a GeminiSEM 300 field emission scanning electron microscope (FE-SEM, ZEISS, Germany) equipped with a Bruker energy-dispersive X-ray spectroscopy (EDX) system for analyzing elemental distribution. Using the soil mode, the elemental compositions of the reclaimed precipitates were recorded using a handheld X-ray fluorescence (XRF) spectrometer of the DELTA series DC-4000 (Olympus, USA).

2.5. Theoretical calculation

To explore the mechanism of struvite formation influenced by various ECs, density functional theory (DFT) calculations were performed using the Gaussian 16 software, version C.01 (Frisch, 1992). Geometry optimization, electrostatic potential (ESP), and energy calculations were conducted for various forms of HA, TC, Cu+TC, and aged PET complex using the hybrid DFT approach at the B3LYP/6 – 31 + G(d, p) calculation level (Ditchfield et al., 1971; Francl et al., 1982; Grimme et al., 2010; Stephens et al., 1994). The Multiwfn program (Lu, 2024; Lu and Chen, 2012) was used for both the ESP and weak interaction analyses based on the interaction region indicator (IRI) approach (Lu and Chen, 2021), and the Visual Molecular Dynamics (VMD, v1.9.3) program was employed for visualization (Humphrey et al., 1996). Dimer and/or trimer calculations were conducted at the B3LYP/6 – 31 + G(d,p) level with D3BJ dispersion correction (Marenich et al., 2009), followed by single-point energy calculations at M06-2X/def2TZVP with D3 dispersion correction to evaluate binding energies (Weigend and Ahlrichs, 2005; Zhao and Truhlar, 2008). Although HA is inherently heterogeneous, the structural unit selected for DFT calculations represents the deprotonated carboxylic and phenolic moieties that dominate HA speciation at pH above 9.0. Since these deprotonated oxygen-donor groups constitute the primary binding sites for Cu^{2+} or Mg^{2+}, we chose a representative HA model that effectively captures the essential coordination chemistry of the Cu^{2+}-HA interface relevant to this study (Christl et al., 2001). Likewise, the speciation of TC at pH ~ 9.5 is dominated by the [TC^{2-}] form given its pKa values of TC (3.3, 7.7, and 9.7) (Gu and Karthikeyan, 2005). Accordingly, this specific protonation state was utilized in the DFT modeling to accurately represent the active binding sites of TC in the experimental system.

3. Results and discussion

3.1. Effect of P loading on crystallization kinetics

The temporal dynamics of struvite crystallization in BRs were

fundamentally characterized by the simultaneous consumption of soluble phosphate ions (PO_4^{3-}-P) and a concomitant reduction in suspension pH, providing a robust indirect metric for monitoring precipitation progress (Nelson et al., 2003). Therefore, we employed a dual-monitoring approach to explore these kinetics, tracking the depletion of soluble phosphate and the evolution of solution pH over time. Theoretically, the initial phosphate concentration (P loading, $[PO_4]_0$) serves as a primary determinant of the system's supersaturation (S), where higher $[PO_4]_0$ values are expected to enhance the thermodynamic driving force and accelerate crystallization kinetics. Our data revealed a consistent trend across all tested P loadings (20 – 250 mg L^{-1}, see supplementary material Fig. S2a,b): both the soluble phosphate concentration and suspension pH decreased rapidly during the initial reaction phase (0–10 min), followed by a period of gradual recession before approaching quasi-equilibrium states at approximately 40 and 20 min for pH and phosphate, respectively. This two-stage kinetic profile—an initial linear decline transitioning to a plateau—is in excellent agreement with our prior findings (Yan et al., 2024; Zahid et al., 2025), confirming that the fundamental progression of crystallization in the present matrix follows a previously established pattern. Notably, the magnitude of the pH decrease from the initial value (~9.5) was positively correlated with the P loading (see supplementary material Fig. S2c). This observation is chemically coherent, as a greater quantity of phosphate ions necessitates the release of a proportionally larger stoichiometric equivalent of protons during its incorporation into the struvite lattice (Bhuiyan et al., 2008), thereby imposing a more pronounced acidification of the reaction medium. This acidification, however, serves as a self-limiting feedback mechanism, as the reduction in OH^- activity and the subsequent shift in phosphate speciation from PO_4^{3-} toward HPO_4^{2-} reduce the instantaneous supersaturation, thereby modulating the overall rate of crystal growth as the reaction progresses toward completion.

To quantitatively elucidate the early-stage kinetics of struvite formation, the phosphate depletion data within the initial 10-minute window (see supplementary material Fig. S2b) were subjected to first-order kinetic modeling using Eq. (2). It is important to note that the first-order rate constants (k) derived from the soluble phosphate depletion data (0–10 min) represent apparent kinetic parameters, which integrates multiple simultaneous microscopic processes, including mass transfer, nucleation, and crystal growth. Consequently, it cannot be used to deconvolute the specific rates of nucleation versus crystal growth, but it can indirectly quantify the overall efficiency of struvite crystallization under different conditions. Attempts to fit the kinetic data with a time scale of 0 to 12 min yielded slightly poor correlations and were thus abandoned (see supplementary material Table S1). The resulting fits (see supplementary material Figs. S2d-g) demonstrate high statistical reliability with linear correlation coefficients (R^2) exceeding 0.92 (Table 1). This strong linearity confirms that, within this initial period, struvite crystallization follows a first-order kinetic mode relative to soluble phosphate concentration. However, a comparative analysis of the derived k values reveals a noteworthy complexity: the k values did not demonstrate a monotonic correlation with increasing P loading (Table 1). This finding appears counterintuitive given that higher $[PO_4]_0$ contributes directly to elevated supersaturation, the primary thermodynamic driver for crystallization. This divergence suggests that while P loading establishes the initial thermodynamic potential, the actual kinetics are not solely a function of PO_4^{3-}-P concentration but are governed by a complex interplay of competing physicochemical factors. Specifically, the increased PO_4^{3-}-P concentration enhances the solution's buffer intensity, which may stabilize the local pH and influence the nucleation rate versus the crystal growth rate. Furthermore, at higher supersaturation levels, the system may transition from a growth-controlled regime to one influenced by primary nucleation bursts or mass transfer limitations at the crystal-liquid interface (Agrawal et al., 2018; Ali and Schneider, 2008).

Table 1
Best-fit kinetic equations and the corresponding parameters (rate constant, ***k***, and correlation coefficients, *R*2) of struvite crystallization in batch reactors with varying contents of impurities derived from the first-order kinetic model within a time range of 0–10 min.

Suspension code	Impurity	Content	First-order kinetic equation	k (h^{-1})	Time range	R^2
$[PO_4]_0$=20 ppm	none	0	$y = -0.168\,x - 1.885$	10.08 ± 0.60	0–10 min	0.986
$[PO_4]_0$=50 ppm	none	0	$y = -0.134\,x - 0.754$	8.04 ± 0.78	0–10 min	0.964
$[PO_4]_0$=120 ppm	none	0	$y = -0.192x + 0.289$	11.52 ± 1.62	0–10 min	0.926
$[PO_4]_0$=250 ppm	none	0	$y = -0.181x + 1.071$	10.68 ± 0.90	0–10 min	0.974
Mg/P = 0.8	none	0	$y = -0.110x - 1.106$	6.60 ± 0.60	0–10 min	0.973
Mg/P = 1.0	none	0	$y = -0.112x - 1.056$	6.72 ± 0.96	0–10 min	0.928
Mg/P = 1.2	none	0	$y = -0.128x - 0.760$	7.68 ± 0.84	0–10 min	0.966
Mg/P = 1.4	none	0	$y = -0.133x - 0.744$	7.98 ± 0.96	0–10 min	0.956
HA = 2 ppm	HA	2 ppm	$y = -0.096x - 0.919$	5.76 ± 0.60	0–10 min	0.961
HA = 10 ppm	HA	10 ppm	$y = -0.080x - 1.060$	4.80 ± 0.30	0–10 min	0.987
HA = 20 ppm	HA	20 ppm	$y = -0.078x - 1.093$	4.68 ± 0.42	0–10 min	0.971
Cu = TC = 0.03 mM	TC, Cu	0.03 mM	$y = -0.114x - 0.927$	6.84 ± 0.60	0–10 min	0.971
Cu = TC = 0.12 mM	TC, Cu	0.12 mM	$y = -0.110x - 0.873$	6.60 ± 0.42	0–10 min	0.984
Cu = TC = 0.24 mM	TC, Cu	0.24 mM	$y = -0.107x - 0.872$	6.42 ± 0.42	0–10 min	0.984

Despite these kinetic complexities, the overall process efficiency was significantly enhanced at higher P loadings, with final phosphate removal efficiencies reaching 60.0%, 80.1%, 92.4%, and 97.2% for initial P loadings of 20, 50, 120, and 250 mg L^{-1}, respectively. This suggests that while the speed (rate constant) of the initial reaction phase may be complexly controlled, the final extent of crystallization is significantly favored by higher initial P loadings.

3.2. *Effect of Mg/P ratio on crystallization kinetics*

The stoichiometric availability of magnesium relative to phosphorus (the Mg/P molar ratio) serves as a primary determinant of the thermodynamic driving force and the subsequent kinetic trajectory of struvite crystallization, exerting a pronounced influence on nucleation rates, crystal growth, and final particle morphology (Nelson et al., 2003). It is well-established that an elevated Mg/P ratio reduces the induction time by enhancing the degree of supersaturation, thereby accelerating nucleation rates and yielding finer crystalline structures due to increased nucleation density (Le Corre et al., 2007; Wang et al., 2020a; Zahid et al., 2025). This fundamental relationship is clearly demonstrated across a Mg/P gradient of 0.8 to 1.4 (see supplementary material Fig. S3).

Specifically, a characteristic triphasic pH evolution was observed across all Mg/P regimes: a rapid, near-linear decline within the initial 10 min, followed by a moderated attenuation between 10 and 35 min, and finally reaching a quasi-equilibrium plateau from 35 to 60 min (see supplementary material Fig. S3a). This three-stage temporal profile of pH serves as an indirect but robust indicator for the fundamental stages of struvite formation. The initial "fast phase" corresponds to the intensive primary nucleation and rapid proton release associated with the deprotonation of NH_4^+ and HPO_4^{2-} species as they are incorporated into the crystal lattice (Yan et al., 2024). Notably, the magnitude of this pH drop was positively correlated with the Mg/P ratio; higher Mg^{2+} dosages facilitated a more pronounced release of H^+ ions, consistent with the stoichiometric consumption of phosphate and the shift in chemical equilibrium (i.e., $H_2PO_4^- \leftrightarrow HPO_4^{2-} + H^+ \leftrightarrow PO_4^{3-} + 2H^+$). In parallel, the depletion of soluble phosphate exhibited a congruent three-stage progression (see supplementary material Fig. S3b), with the residual PO_4^{3-}-P at equilibrium inversely proportional to the applied Mg/P ratio (e.g., 9.08 mg L^{-1} (Mg/P = 1.4) versus 9.60 mg L^{-1} (Mg/P = 1.2), 11.44 mg L^{-1} (Mg/P = 1.0), and 16.94 mg L^{-1} (Mg/P = 0.8)). This signifies that the excess of Mg^{2+} ions effectively shifted the solubility product equilibrium toward the solid phase, thereby facilitating struvite crystallization (Liu et al., 2018). Further analysis pinpointed a distinct "kinetic window" (9.4 – 9.1, highlighted with a pair of red dashed lines) wherein phosphate removal kinetics were most rapid (see supplementary material Fig. S3c). This specific pH window demarcates the transition from metastable supersaturation to rapid crystal proliferation, offering compelling secondary evidence that it encapsulates the critical nucleation burst, during which solution supersaturation is precipitously depleted.

Kinetic modeling reveals that struvite crystallization conforms to the same first-order rate law across all Mg/P regimes (see supplementary material Fig. S4). This is statistically substantiated by the high correlation coefficients ($R^2 > 0.93$, Table 1), implying that the rate-limiting step for earlier struvite crystallization is linearly dependent on the soluble phosphate concentration, consistent with a growth process controlled by mass transfer or surface reaction (Nelson et al., 2003). Note that a clear monotonic increase in the rate constants was observed as the Mg/P ratio progressed from 0.8 to 1.4 (k(Mg/P = 0.8) < k(Mg/P = 1.0) < k(Mg/P = 1.2) < k(Mg/P = 1.4), Table 1), strengthening the role of Mg^{2+} acting as a kinetic accelerator in the crystallization process of struvite (Le Corre et al., 2007). The increase in k values with Mg^{2+} enrichment can be interpreted as a reduction in the activation energy required for the formation of critical nuclei (Wu et al., 2022). By manipulating the Mg/P ratio, it is possible to tailor not only the efficiency of phosphate removal but also the temporal requirements of the treatment process, ensuring that the system operates within the high-speed nucleation regime identified in the pH 9.4–9.1 interval. For comparison, we maintained a 1:1 Mg/P ratio in the subsequent kinetic experiments to examine the impact of ECs.

3.3. Effects of HA and Cu/TC on crystallization kinetics

While our previous studies have established that high concentrations of HA induce strong kinetic and thermodynamic inhibition of struvite and K-struvite formation (Yan et al., 2024; Zahid et al., 2025)—likely through intense HA-Mg^{2+} complexation that alters precipitate size, shape, and phase—the specific impacts of low-level HA (0–20 mg L^{-1}) on early-stage kinetics remain less defined. Herein, we observed that, unlike high-load scenarios, low concentrations of HA resulted in negligible changes to temporal pH profiles during the initial 0–10 min of reaction (see supplementary material Fig. S5a), a phenomenon likely explained by the negligible buffering capacity of HA at low concentrations in this alkaline medium (Zahid et al., 2025). However, the inhibitory role of HA became pronounced in the subsequent growth phase (10–30 min), where HA presence catalyzed a faster pH decline compared to the control. This behavior suggests a rapid release of H^+ ions resulting from the chelation of Mg^{2+} by HA, a mechanism that possibly competes with the struvite lattice for magnesium (Wang et al., 2024; Yan et al., 2024). This competition was corroborated by elevated soluble phosphate concentrations (20.60 mg L^{-1} versus 9.60 mg L^{-1} for HA = 20 ppm and blank, see supplementary material Fig. S5b) and a delayed equilibrium time (40 min in the matrix with 20 mg L^{-1} of HA versus 30 min in the blank, see supplementary material Fig. S5b). Furthermore, this inhibition constricted the optimal pH window to 9.4–9.2 (see supplementary material Fig. S5c). Despite these perturbations, the crystallization followed well-defined first-order kinetics ($R^2 > 0.96$, see supplementary material Fig. S6), with k values notably decreasing from 8.04 (blank) to 4.78 (HA = 20 ppm) (Table 1). To further evaluate whether Mg^{2+} complexation could account for the inhibitory effects of HA, speciation calculations were performed using Visual MINTEQ 3.1 under the experimental conditions (i.e., HA = 10 ppm, pH = 9.5, and total Mg concentration = 1.614 mM). The target crystalline phase was not allowed to precipitate in the model, so that the calculated speciation reflected the initial solution chemistry before struvite crystallization. Notably, the calculated free Mg^{2+} activity was decreased by only 1.27% in the presence of 10 ppm HA relative to the control matrix (see supplementary material Fig. S7 and Table S2), suggesting that Mg^{2+} complexation alone is unlikely to fully explain the inhibitory impact of HA on struvite crystallization at relatively low dosage. In fact, HA may inhibit struvite crystallization through several surface-mediated pathways: i) adsorption onto active crystal faces, thereby blocking growth sites and hindering the incorporation of Mg^{2+}, NH_4^+, and PO_4^{3-} into the crystal lattice; ii) regulating the surface charge of nuclei or growing crystals, increasing electrostatic repulsion and reducing particle aggregation; iii) introducing steric hindrance near the crystal surface and stabilizing amorphous or poorly crystalline precursor phases, thus delaying their crystallization (Ge et al., 2020; Wu et al., 2022; Zhang et al., 2016). Therefore, the inhibitory effect of HA is more likely to be a combined result of these surface-mediated processes and weak Mg^{2+} complexation.

The crystallization matrix was further challenged by the introduction of Cu^{2+} and TC, which exhibited inhibitory patterns analogous to HA (Fig. 2). The presence of Cu and TC yielded similar temporal trends in pH decay and phosphate consumption (Fig. 2 a,b), resulting in a similar postponement of the equilibrium time to 45 min (Fig. 2 b) and a comparable contraction of the optimal pH window to 9.4–9.2 (Fig. 2 c). Fitting results confirmed that struvite crystallization maintained first-order kinetics within the initial 10 min despite the presence of these contaminants ($R^2 > 0.97$, Fig. 2 d), with k values decreasing in the order of 8.04 (blank) > 6.84 (Cu = TC = 0.03 mM) > 6.60 (Cu = TC = 0.12 mM) > 6.42 (Cu = TC = 0.24 mM) (Table 1). A counterintuitive phenomenon was observed during the growth stage (>10 min), where the inhibition of struvite growth appeared inversely proportional to the concentration of the Cu+TC mixture (Fig. 2b). Specifically, lower levels of Cu+TC exerted a more potent inhibition on struvite growth than higher levels. This may be attributed to speciation dynamics: at lower concentrations, the specific inhibitory effects of Cu^{2+} and TC species may be physically restricted by the abundance of surrounding Mg^{2+} ions (Wang et al., 2024). Conversely, at higher levels, the thermodynamically favorable chelation of Cu^{2+} by TC (due to TC's higher affinity for Cu^{2+} over Mg^{2+}) may diminish the availability of free inhibitory ions, thereby reducing their interference with crystal growth. Similarly, speciation calculations of Mg^{2+} in the presence of 0.12 mM Cu+TC were conducted as well (see supplementary material Fig. S7 and Table S2). The results showed that the calculated free Mg^{2+} activity was decreased by 7.98% in the presence of Cu+TC, indicating that TC-containing species exhibit a strong tendency to bind Mg^{2+}. However, its overall Mg-complexation capacity was limited due to its much lower dosage compared to Mg^{2+} (0.12 versus 1.614 mM). Therefore, Mg^{2+} complexation by Cu-TC may contribute to the inhibition, but it is unlikely to be the dominant

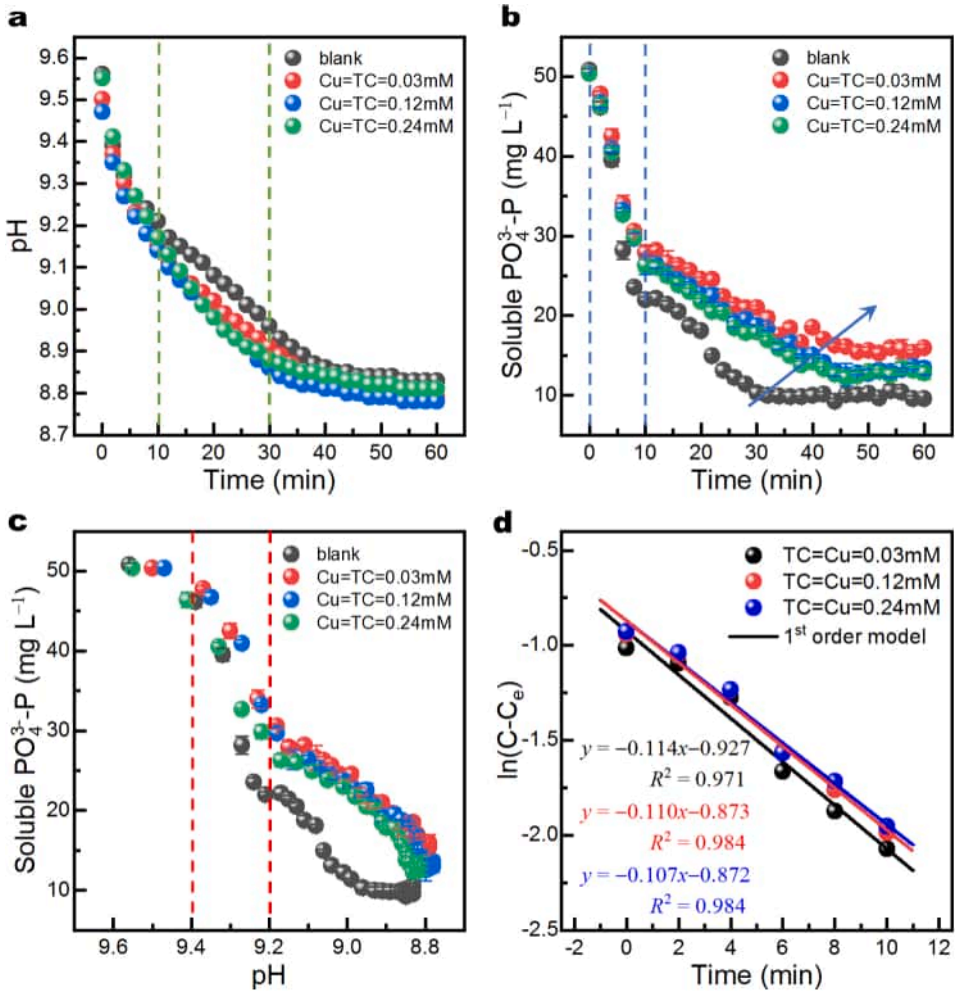

Fig. 2. (**a**) Temporal profiles of pH, (**b**) Temporal profiles of soluble PO_4^{3-}-P (the blue parallel dash lines define the data for kinetic fitting; the blue arrow line highlights the extension of crystal growth duration due to the inhibitory effects of Cu+TC), (**c**) Plots of soluble PO_4^{3-}-P versus pH during the struvite crystallization in BRs ($[PO_4]_0$ = 50 mg L^{-1}, initial pH = 9.5) with varying contents of Cu and TC (the red parallel dash lines in panel **c** highlight the pH window between 9.4 and 9.2 wherein the soluble PO_4^{3-}-P dropped at the fastest rate, corresponding to the initial rapid nucleation stage of struvite); (**d**) Kinetic linear fitting plots of soluble PO_4^{3-} in suspensions with 0.03, 0.12, and 0.24 mM of equimolal Cu and TC.

mechanism.

Collectively, these results highlight the varying impacts of these ECs on phosphate recovery— PET promotes formation by reducing energy barriers (Yan et al., 2024), while HA and Cu-TC may affect struvite crystallization partly by reducing the effective availability of Mg^{2+}. However, the Visual MINTEQ results suggest that Mg^{2+} complexation alone cannot fully account for the observed inhibition, especially at the relatively low dosages. Other mechanisms, including adsorption onto active crystal faces, surface-charge modification, steric hindrance, and stabilization of amorphous or poorly crystalline precursor phases, are also likely involved (Ge et al., 2020; Wu et al., 2022; Zhang et al., 2016).

3.4. *Effects of HA and Cu/TC on precipitates reclaimed from BRs*

Beyond the established influence on crystallization kinetics, a critical imperative in phosphorus recovery is assessing the physicochemical quality of the reclaimed struvite, particularly when generated from matrices impaired by various ECs. To rigorously evaluate this, precipitate harvesting from the BRs was isolated and characterized in both the absence and presence of target contaminants (Fig. 3). A stark dichotomy in crystallographic integrity was observed depending on the coexisting ECs. As illustrated in Fig. 3a, the introduction of HA induced a significant deterioration in crystallinity (BR-HA), evidenced by the broadening of diffraction peaks and an elevated amorphous background in the BR-HA diffractograms compared to the BR-blank. Conversely, the co-presence of Cu^{2+} and TC (Cu+TC) unexpectedly promoted the development of a highly ordered struvite crystal. This is substantiated by the intensification of the characteristic reflections at (1 1 1), (0 0 2), and (1 0 1) of struvite (JCPDS #71–2089) relative to the blank sample (BR-blank). This finding uncovers an intriguing physicochemical paradox: while Cu+TC acts as a kinetic inhibitor by retarding the nucleation rate (Fig. 2 b), it concurrently creates a thermodynamic environment that preferentially selects for high-quality struvite crystals once nucleation is overcome, effectively acting as a “quality catalyst”.

To quantify these variations in phase purity, Whole Pattern Fitting (WPF) calculations were employed (Fig. 3 b). The analysis confirmed that the struvite phase remained dominant across the samples but exhibited varying degrees of purity, decreasing in the order of BR-Cu+TC (99.7%) > BR-blank (97.0%) > BR-HA (32.7%). This compositional analysis was further corroborated by vibrational spectroscopy (Fig. 3 c), where the fingerprint infrared bands corresponding to NH_4^+ bending vibrations (1610 cm^{-1} and 1445 cm^{-1}) and P-—O stretching vibrations (~1000 cm^{-1} and 572 cm^{-1}) aligned precisely with our previous characterization of high-purity struvite (Bah et al., 2023). Moreover, microscopic analysis reveals that the presence of these ECs exerted a profound influence on crystal morphology (Fig. 3 d–f). While the blank

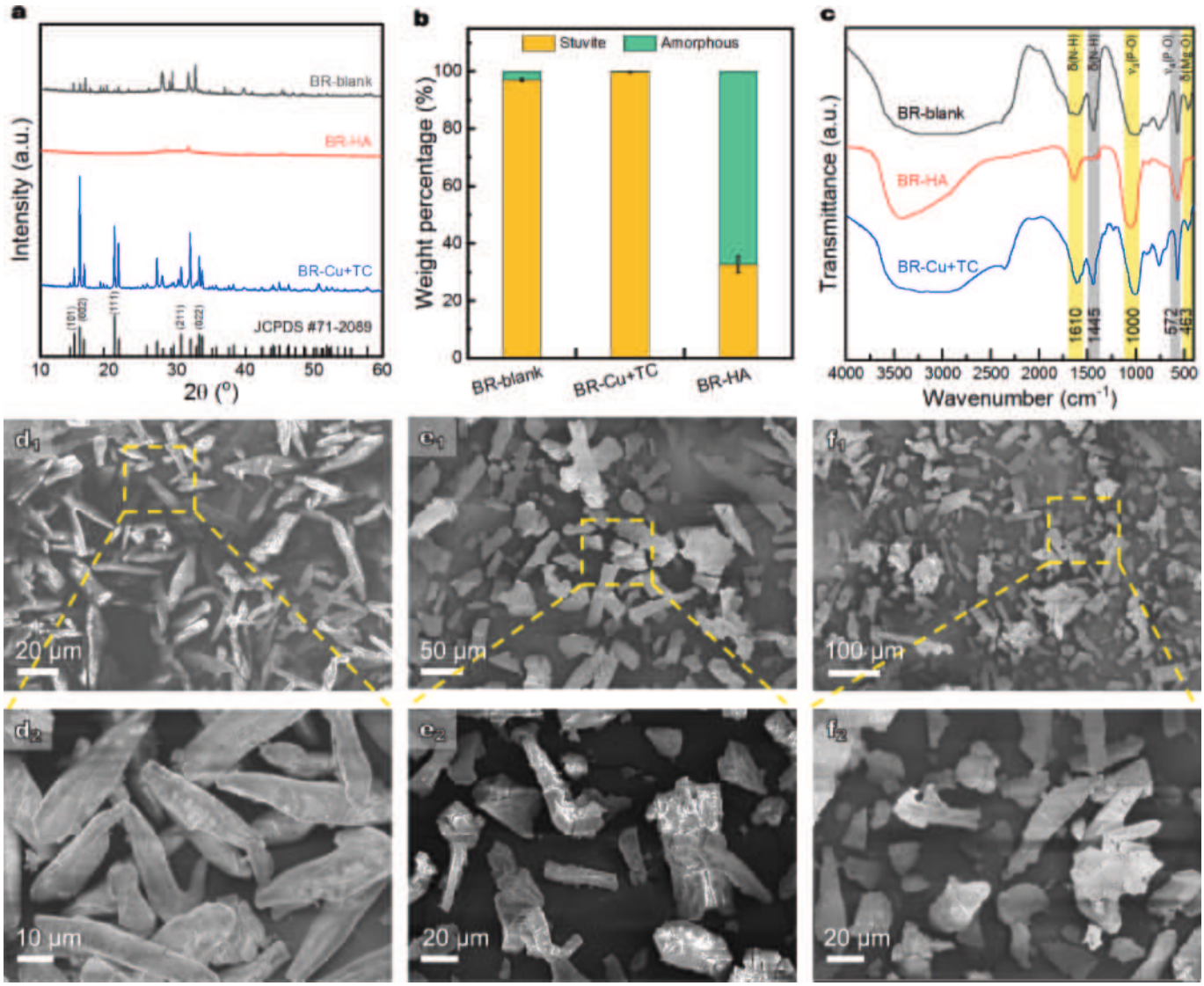

Fig. 3. Characterization of struvite reclaimed from BRs: (**a**) XRD patterns (struvite, JCPDS #71–2089), (**b**) phase composition, (**c**) FTIR spectra, (**d-f**) SEM images of (**d_1**, **d_2**) blank, (**e_1**, **e_2**) BR-HA (i.e., precipitate in the presence of 10 mg L^{-1} of HA), and (**f_1**, **f_2**) BR-Cu+TC (i.e., precipitate in the presence of 0.12 mM Cu and TC) at varying magnification levels.

matrix yielded precipitates with a uniform, shuttle-like morphology (Fig. 3 d) typically observed in BR systems (Le Corre et al., 2005; Liu and Wang, 2019), the introduction of ECs induced a distinct morphological shift. Both HA and Cu+TC matrices yielded precipitates dominated by prismoid or rod-like particulates (Fig. 3 e,f). This morphological evolution is likely driven by the specific chelation of Mg^{2+} ions by HA or TC functionalities, which alters the growth rates of specific crystal faces (Hu et al., 2022). This aligns with our prior findings where co-occurring microplastics (PET) facilitated the growth of short, prism-shaped struvite (Yan et al., 2024), collectively underscoring that while ECs exert varying influences on phase composition, they universally modulate the morphological trajectory of the recovered struvite product, with Cu+TC uniquely enhancing phase purity despite its kinetic inhibition.

3.5. *Effects of HA, Cu/TC, and PET on precipitates reclaimed from FBRs*

The transition from BRs to FBRs fundamentally altered the crystallization landscape, leveraging a prolonged hydraulic retention time (HRT, 3 d in FBRs versus 1 h in BRs) to facilitate the development of superior crystalline structure. This is evidenced by the significantly higher reflection intensities in the XRD pattern of FBR-blank precipitates compared to BR-blank (cf. Figs. 3 a, Fig. 4 a). Furthermore, the inherent circulation and fluidization within the FBR increased the collision probability of nascent crystals, promoting both crystal growth and conglomeration into larger, near-spherical pellets (see supplementary material Figs. S8, S9). Specifically, the recirculation flow of 50 mL min^{-1} and corresponding upflow velocity of 9.55 m h^{-1} induced sufficient shear stress and particle collision within the FBR. This hydrodynamic environment likely facilitated the abrasion of the pellet surface, preventing the localized accumulation and surface poisoning of Cu-TC complexes that kinetically inhibit crystal growth. Furthermore, the high recirculation ratio (500%) ensured vigorous macro-mixing and enhanced the mass transfer of bulk phosphate, NH_4^+, and Mg^{2+} ions to the pellet surface (Lou et al., 2018). This enhanced convective transport likely helped overcome the diffusion limitations imposed by the Cu-TC complexes, thereby sustaining the apparent crystallization rate and promoting the incorporation of contaminants into the pellet matrix (Gao et al., 2023). Unlike the smaller and less crystalline particles obtained from the 1-hour batch experiments (Fig. 3 a, d–f), the combined effects of extended HRT and favorable hydrodynamics resulted in highly crystalline, larger, and conglomerated struvite pellets (97.3% purity) (Fig. 4 b–d). Cross-sectional analysis revealed these FBR-blank pellets (Φ ~

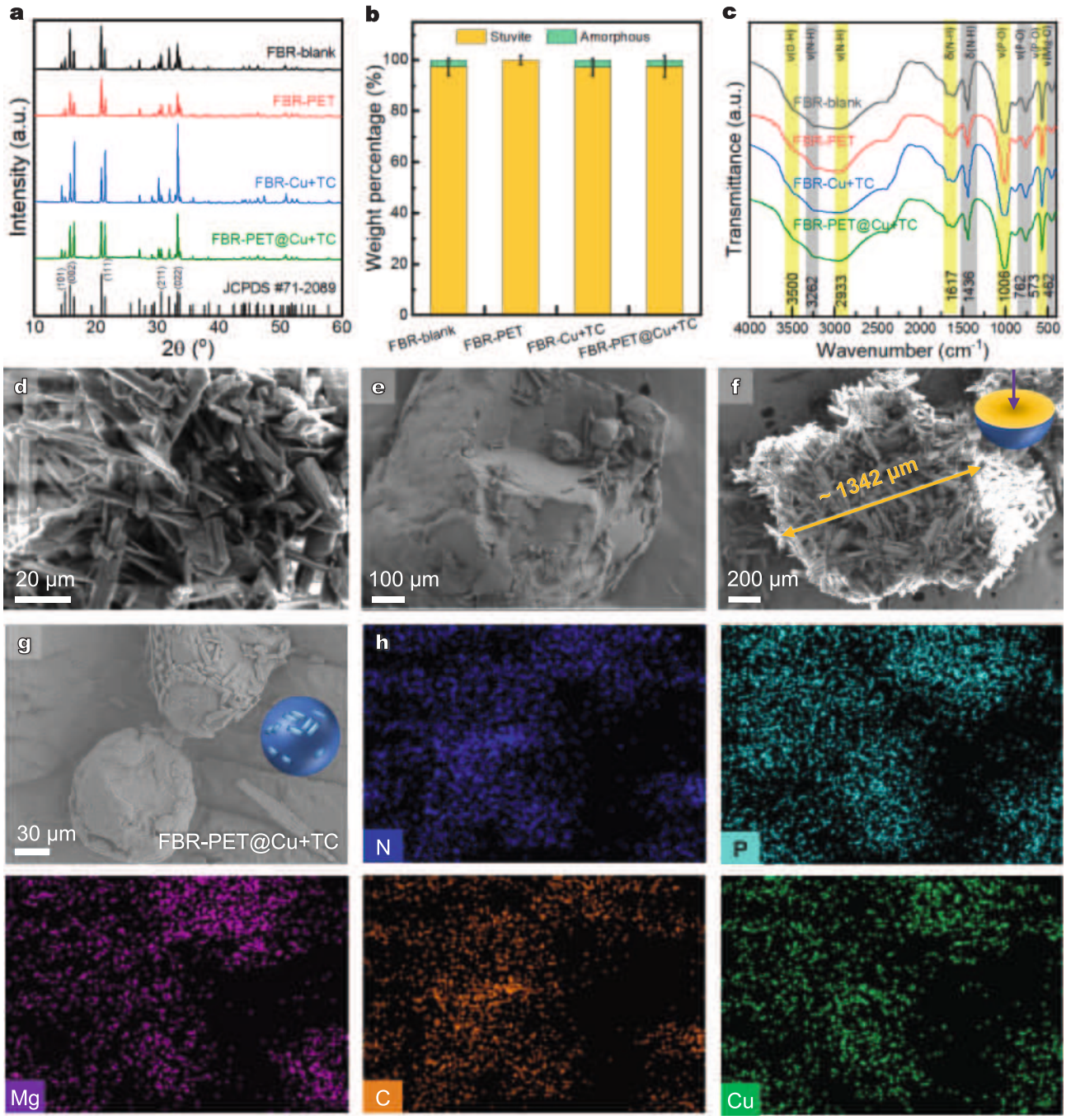

Fig. 4. Characterization of struvite reclaimed from FBRs: (**a**) XRD patterns, (**b**) phase composition, (**c**) FTIR spectra, (**d-g**) SEM images of (**d**) blank, (**e**) FBR-PET (i.e., precipitate in the presence of PET), (**f**) cross-section of FBR-Cu+TC with diameter ~ 1342 μm (i.e., precipitate in the presence of 0.12 mM Cu and TC; the inset depicts the cross-section illustration of the struvite pellet), (**g**) FBR-PET@Cu+TC (i.e., precipitate in the presence of Cu+TC-loaded PET, the inset depicts the illustration of the attaching and stacking of Cu+TC-induced rodlike struvite over the surface of PET-induced spherical struvite pellets), and (**h**) EDX elemental mapping of the area shown in panel **g**.

1138 μm) to be conglomerates of interlocked rod-shaped crystals with uniformly distributed Mg, N, and P (see supplementary material Fig. S9), a direct result of the enhanced collision frequencies inherent to the FBR hydrodynamics (Shim et al., 2020). This baseline quality was further modulated by the introduction of foreign nuclei. The addition of PET acted as a highly effective seed, boosting phase purity to 100% and templating the growth into dense, PET-like bulk pellets (Figs. 4 a,e, S10, S11). This confirms the "seeding effect" where the morphological memory of the seed dictates the final crystal habit (Yan et al., 2024). Similarly, the Cu+TC complex, despite its kinetic inhibition in batch modes, promoted crystallinity in the FBR and facilitated the formation of even larger conglomerates (Φ ~ 1342 μm, see supplementary material Fig. S12) through likely bridge-complexation mechanisms (Ma et al., 2024; Rouff et al., 2016). When combined (FBR-PET@Cu+TC), the system benefited from both effects: the PET seeds maintained high purity (97.5%) and induced a compact near-spherical morphology, while the Cu+TC influenced surface deposition, resulting in PET cores coated with rod-like struvite crystals (Fig. 4 g). Nevertheless, intentional use of PET as seeds should be dissentient due to the nature of "pollutant vector" of such microplastics (Wang et al., 2020b) and the potential agronomic safety issues.

Beyond physical characterization, understanding the chemical fate

of co-occurring contaminants is vital for safe nutrient recovery. EDX elemental mapping and XRF analyses of the FBR-Cu+TC pellets indicated a disproportionate enrichment of Cu^{2+} relative to TC within the struvite matrix (see supplementary material Figs. S12, S13). Nevertheless, it is important to recognize the limitations of these techniques. They cannot definitively distinguish between true lattice encapsulation, surface adsorption, physical entrapment within pellet micropores, and association with amorphous phase boundaries. Cross-sectional SEM line-scan analysis would be required to unequivocally confirm internal encapsulation. Therefore, the observed Cu enrichment likely reflects a combination of these mechanisms. Interestingly, the presence of PET altered this sequestration dynamic; the compact nature of PET-induced pellets facilitated the incorporation of Cu^{2+} within the struvite spheroid pellet matrix (see supplementary material Figs. S13, Fig. 4g), effectively immobilizing the metal and lowering the risk of secondary environmental exposure. However, the efficacy of the FBR system faced significant limitations when applied to real swine wastewater. The resulting precipitates were predominantly amorphous phosphate bulks (84.9%) rather than crystalline struvite (see supplementary material Figs. S14, S15). This degradation in product quality is attributed to the high burden of dissolved organic matter (DOM, ~271 mg L^{-1}) and Ca^{2+} ions in the real matrix (see supplementary material Table S3), both of which are known to hinder struvite nucleation and growth by blocking active sites and competing for phosphate species (Le Corre et al., 2005; Liu and Wang, 2019; Lou et al., 2018). These findings highlight a critical operational boundary: while engineered FBR systems and seeding agents like PET can optimize recovery in synthetic or semi-synthetic waters, the successful valorization of nutrient-rich real waste streams necessitates upstream interventions to neutralize the inhibitory effects of DOM and calcium ions (Bayuseno and Schmahl, 2020; Chen et al., 2026; Gao et al., 2023).

3.6. DFT calculations and impacts of various ECs on struvite crystallization

Density Functional Theory (DFT) calculations were employed to provide vital theoretical insights into the subtle molecular interactions between struvite constituent ions and diverse ECs. Understanding the quantum–mechanical nature of these molecular interactions is highly critical, as it explains the macroscopic impacts of such heterogeneous impurities on both the reaction kinetics of struvite precipitation and the potential agronomic safety of the final recovered mineral products (Gao et al., 2024a; Gao et al., 2023). A cornerstone of this analysis was the generation of electrostatic potential (ESP) contour maps for each EC, which, following geometry optimization, allowed for the precise identification of potential reaction sites (Gao et al., 2024b). These contour maps, with labeled extreme points in Fig. 5, reveal the exact locations where oppositely charged ions are most likely to bind. For instance, the fully deprotonated humic acid (HA^{3-}, prevalent at pH > 9.5) displays its most negative ESP minima loci between two carboxyl groups (=COO^{2-}, Fig. 5 a), with energies of −285.2 and −283.4 kcal mol^{-1}, marking them as the primary thermodynamically active coordinate sites for cations like Mg^{2+}. Similarly, the ESP minima for deprotonated tetracycline species (HTC^{-}, TC^{2-}) and their copper complexes (CuTC, CuTC2) are consistently localized between two neighboring phenol diketone moieties (Fig. 5 b-e). Likewise, an aged PET fragment showed its most negative ESP loci (−201.9 kcal mol^{-1}) at its terminal carboxyl group (Fig. 5 f). Consequently, these functionally localized groups serve as the most active heterogeneous binding sites for sequestering dissolved Mg^{2+} ions away from the primary struvite formation pathways.

The predictive power of the ESP analysis was confirmed by calculating the binding energies (BEs) for dimer complexes of $Mg[H_2O]_6^{2+}$ and $Cu[H_2O]_6^{2+}$ with the ECs (Fig. 6, S16-18). The complexation of Mg^{2+} with HA and aged PET resulted in relatively low BEs of −24.412 and −36.866 kcal mol^{-1}, respectively (Figs. 6 a, S17a), characterized by weak Mg−O coordination. In contrast, the Mg-TC dimer exhibited a substantially higher BE of −47.974 kcal mol^{-1} (Fig. 6 b), attributed to the synergistic effect of a weak coordinate bond and a strong hydrogen bond. This stronger interaction aligns with previous reports that Mg^{2+} can facilitate the residual enrichment of TC in struvite (Gao et al., 2024b). For Cu^{2+}, the trend was similar but with greater magnitudes. Specifically, the Cu-HA interaction remained weak (BE = -26.330 kcal mol^{-1}, see supplementary material Fig. S17c), while Cu-aged PET and Cu-TC formed significantly more stable dimers with BEs of − 49.143

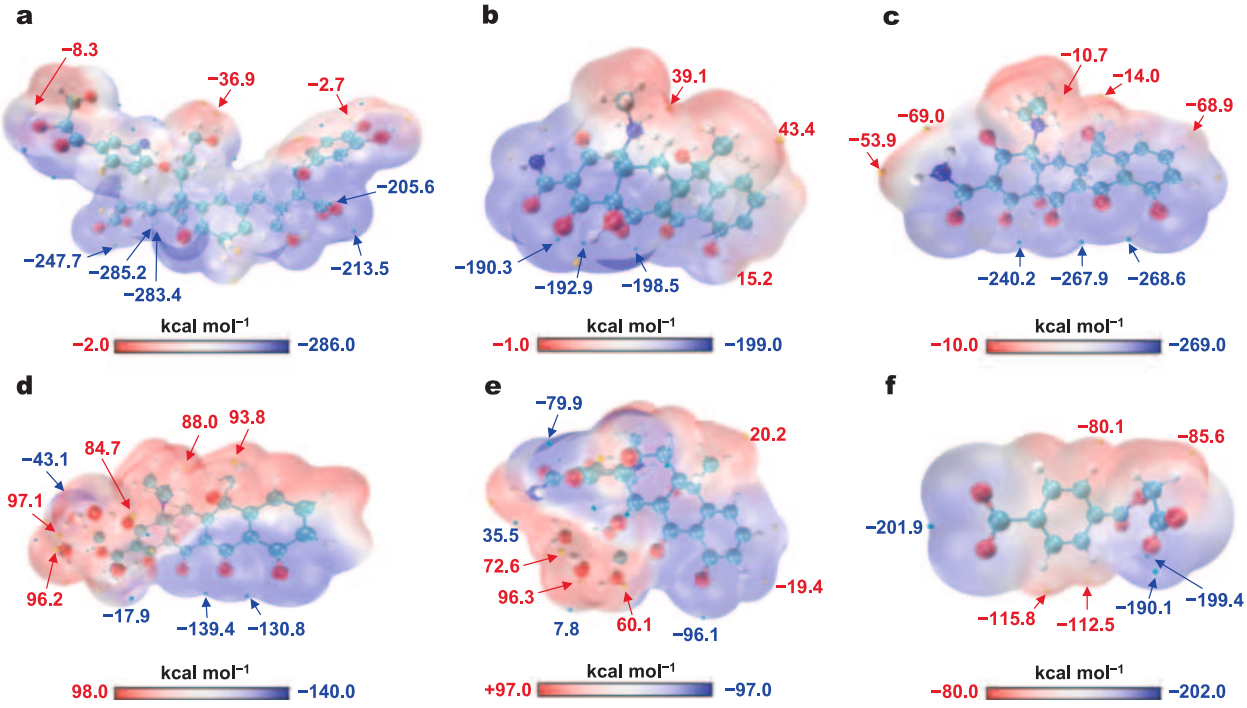

Fig. 5. ESP contour maps of (**a**) HA^{3-}, (**b**) HTC^{-}, (**c**) TC^{2-}, (**d**) CuTC, (**e**) CuTC2, and (**f**) aged PET. The gray, while, red, blue, and cyan colors represent the C, H, O, N, and Cu atoms, respectively. Note that the two DFT-optimized CuTC dimers (**d**, **e**) show different ESP distributions due to their distinct configurations.

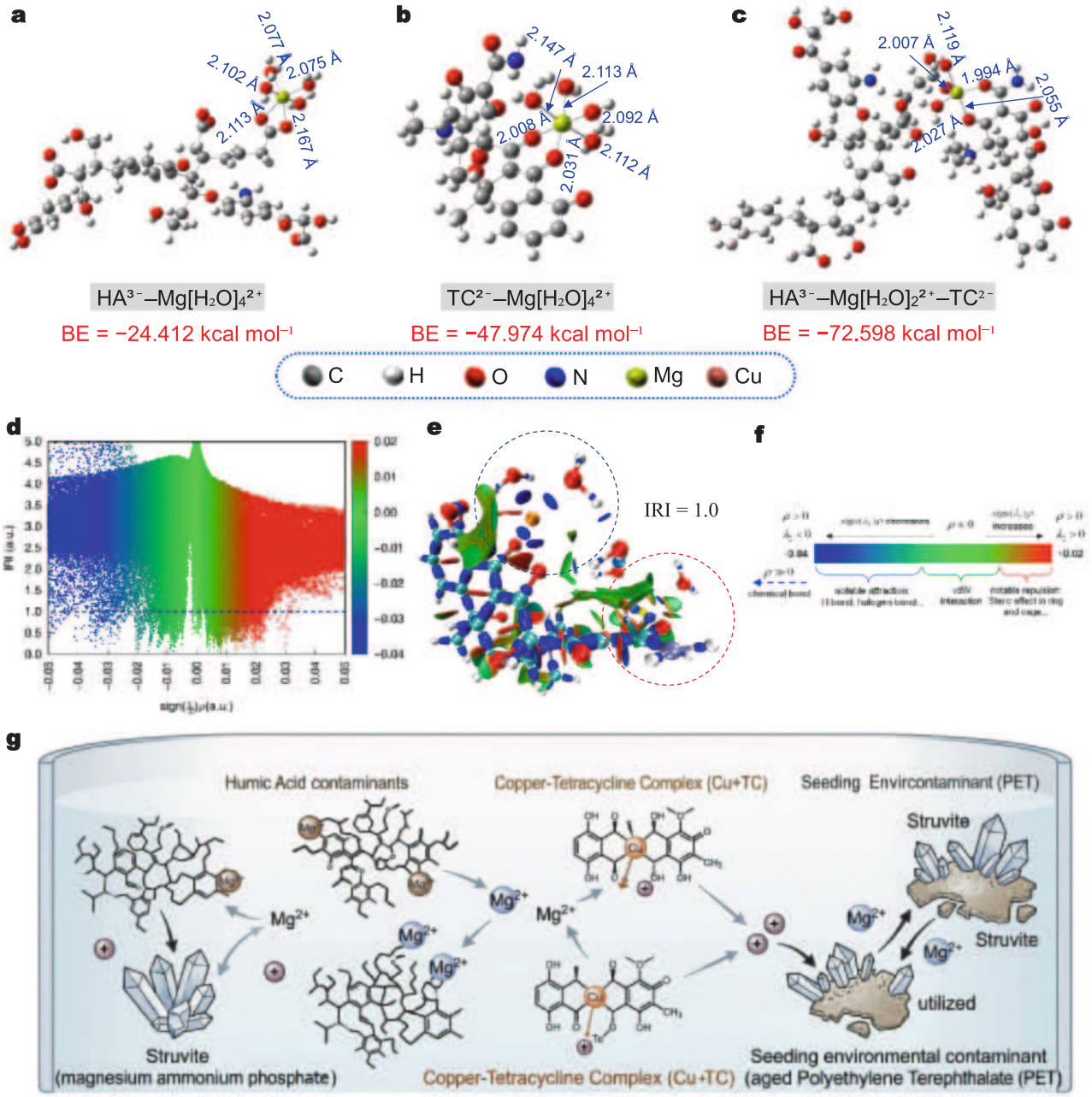

Fig. 6. (a–c) Optimized configurations, relevant binding energies and Mg–O bond lengths of different complexes: (a) HA^{3-}–$Mg[H_2O]_4^{2+}$ dimer, (b) TC^{2-}-$Mg[H_2O]_4^{2+}$ dimer, and (c) HA^{3-}–$Mg[H_2O]_4^{2+}$–TC^{2-} trimer. Notably, the Mg−O bridge complexation contributed to the enhanced stability of the HA^{3-}–$Mg[H_2O]_4^{2+}$–TC^{2-} trimer, as indicated by the relatively low BE (−72.598 kcal mol^{-1}). (d) Scatter map of IRI versus sign(λ_2)ρ and (e) the corresponding isosurface map of IRI = 1.0 of HA^{3-}–$Mg[H_2O]_4^{2+}$–TC^{2-} trimers, (f) the standard IRI colorbar and chemical explanation (Lu and Chen, 2021). Note that the blue spikes within the sign(λ_2)ρ range of − 0.04 to − 0.03 correspond to the interactions between the Mg^{2+} or Cu^{2+} and the surrounding O within the dashed line circle, which appears to be weak coordination interaction (M−O), the green spikes above − 0.02 are connected to the weak van der Waals (vdW) interactions, and the red spikes above 0.00 correspond to the steric effect among the terminal groups within HA or TC (see supplementary material Table S4–S6). (g) Schematic illustration of the specific impact of these ECs on struvite crystallization, with HA and Cu+TC acting as inhibitors by engaging in weak to moderate coordination interactions with free Mg^{2+} ions, whereas aged PET also exhibits weak coordination with Mg^{2+}; its role as a solid particulate introduces a profound seeding effect, overshadowing its minor Mg^{2+}-complexing capacity. This graphic was created with the assistance of Google Gemini Image 2.5.

and − 65.169 kcal mol^{-1}, respectively (see supplementary material Fig. S17b,d), due to the formation of classical Cu–O coordinate bonds and strong H-bonds. The stability of these Cu complexes suggests they are potential vectors for the incorporation of both the metal and the organic ligand into the struvite matrix (Wang et al., 2020c). Further confirmation of the bonding nature came from IRI and atoms-in-molecules (AIM) topological analyses (see supplementary material Fig. S19, Tables S3-5). These methods confirmed that the Mg^{2+}-HA and Mg^{2+}-aged PET interactions are non-covalent, dominated by ion–dipole forces (see supplementary material Fig. S19 a–d), perfectly mirroring their BE data (Fig. 6 a, S17a).

Real-world wastewater matrices are complex, containing a mixture of ECs. To simulate this, we extended our DFT calculations to trimer configurations. Our findings reveal that in mixtures containing HA, TC, and either Mg^{2+} or Cu^{2+}, the metal ions frequently act as bridges, forming stable ternary complexes such as HA-Mg-TC and aged PET-Mg-TC

(Fig. 6c, S18). This metal-O bridging complexation mechanism provides a direct pathway for the co-enrichment of multiple ECs within the same precipitate (Gao et al., 2024b), potentially exacerbating the risk of these ECs' spreading. However, the dynamics become more intricate when two different metal ions compete for the same ligand. In the Cu-TC-Mg trimer, the calculated BE dropped to −30.779 kcal mol^{-1} (see supplementary material Fig. S18), indicating that competition between Cu and Mg for the primary binding sites on TC leads to a less stable and potentially less favored configuration compared to the Cu-TC dimer. IRI and AIM topological analyses also confirm that the Cu-TC-Mg system features both strong covalent Cu–O bonds and weaker Mg−O coordination (Fig. 6 d,e). This suggests that in systems with competing metals, the speciation and fate of ECs will be governed by the relative affinities and concentrations of all species present (Huang et al., 2021).

Synthesizing the DFT and above macroscopic results allows us to sketch ECs and their impacts on struvite formation (Fig. 6 g). Specifically, soluble ECs like HA and CuTC primarily act as inhibitors by engaging in weak to moderate coordination interactions with free Mg^{2+} ions, effectively reducing the supersaturation with respect to struvite. In contrast, while aged PET also exhibits weak coordination with Mg^{2+}, its role as a solid particulate introduces a profound seeding effect (Yan et al., 2024). Its ability to serve as a nucleation seed likely overshadows its minor Mg^{2+}-complexing capacity, leading to an overall acceleration of crystallization kinetics (Yan et al., 2024). In the most complex, multi-EC scenarios, our results point towards the preferential formation of metal-bridged trimeric complexes. The net effect on struvite crystallization—whether inhibition or promotion—would then be a balance between the sequestering of ions by these large complexes and any seeding effect from particulate matter like aged PET. This balance ultimately dictates the fate of ECs, possibly promoting their enrichment in the reclaimed precipitates and thus raising potential agronomic safety issues, which need to be further explored by standard leaching tests and quantitative risk assessment in future studies from a practical perspective.

4. Conclusions

By employing a coupled experimental strategy that bridges fundamental crystallization kinetics (via batch reactors) with continuous fluidized-bed reactors and DFT calculations, we elucidate the distinct mechanisms through which emerging contaminants (PET, TC, Cu^{2+}, and HA) modify crystal formation. Batch experiments revealed that ECs alter apparent kinetic parameters, with Cu+TC and HA exhibiting pronounced inhibitory effects on nucleation and growth rates, while PET demonstrated a kinetic accelerator. In parallel, FBR experiments contextualized these effects under continuous-flow conditions, demonstrating that the extended hydraulic retention time and enhanced collision frequency can partially offset kinetic suppression observed in batch regimes. Critically, by combining with theoretical calculation results, we identify mechanistic thresholds: PET functions as a passive morphological template and seed promoting crystallization kinetics, whereas the Cu+TC complex actively modifies agglomeration pathways through bridge complexation, enhancing pellet size while preferentially incorporating Cu over TC into the struvite matrix in FBR platforms. Humic acid, conversely, imposes kinetic poisoning across both regimes, suppressing crystallinity through a combination of surface-mediated interactions and weak Mg^{2+} complexation. The translation to real swine wastewater revealed that elevated dissolved organic matter and Ca^{2+} exceed critical inhibitory thresholds, inducing amorphous phosphate formation. Consequently, resilient phosphorus recovery requires integrated strategies—combining pre-treatment to remove strong inhibitors with applied FBR conditions. Future efforts must prioritize robust pre-treatment technologies capable of selectively removing these key inhibitors, thereby unlocking the full potential of FBR crystallization for nutrient recovery from complex waste streams.

CRediT authorship contribution statement

Xianfei Wang: Writing – original draft, Validation. **Degui Gao:** Visualization, Validation. **Mengyu Ma:** Validation, Investigation. **Ruxin Han:** Visualization. **Bing Li:** Validation, Resources, Supervision. **Dawei Li:** Resources. **Feihu Li:** Writing – review & editing, Writing – original draft, Visualization, Supervision, Conceptualization.

Declaration of competing interest

The authors declare that they have no known competing financial interests or personal relationships that could have appeared to influence the work reported in this paper.

Acknowledgments

The work was partially supported by the Priority Academic Program Development (PAPD) of Jiangsu Higher Education Institutions.

Appendix A. Supplementary data

Supplementary data to this article can be found online at https://doi.org/10.1016/j.biortech.2026.135390.

Data availability

Data will be made available on request.

References

Agrawal, S., Guest, J.S., Cusick, R.D., 2018. Elucidating the impacts of initial supersaturation and seed crystal loading on struvite precipitation kinetics, fines production, and crystal growth. Water Res. 132, 252–259. https://doi.org/10.1016/j.watres.2018.01.002.

Ali, M.I., Schneider, P.A., 2008. An approach of estimating struvite growth kinetic incorporating thermodynamic and solution chemistry, kinetic and process description. Chem. Eng. Sci. 63 (13), 3514–3525. https://doi.org/10.1016/j.ces.2008.04.023.

Bah, A.T., Shen, Z.Y., Yan, J.N., Li, F.H., 2023. Phosphorous recovery from water via batch adsorption enrichment combined with struvite crystallization in a fluidized bed reactor. J. Environ. Chem. Eng. 11 (3), 110180. https://doi.org/10.1016/j.jece.2023.110180.

Bayuseno, A.P., Schmahl, W.W., 2020. Crystallization of struvite in a hydrothermal solution with and without calcium and carbonate ions. Chemosphere 250, 126245. https://doi.org/10.1016/j.chemosphere.2020.126245.

Bhuiyan, M.I.H., Mavinic, D.S., Beckie, R.D., 2008. Nucleation and growth kinetics of struvite in a fluidized bed reactor. J. Cryst. Growth 310 (6), 1187–1194. https://doi.org/10.1016/j.jcrysgro.2007.12.054.

Chan, R., Chiemchaisri, C., Chiemchaisri, W., Boonsoongnern, A., Tulayakul, P., 2022. Occurrence of antibiotics in typical pig farming and its wastewater treatment in Thailand. Emerging Contam. 8, 21–29. https://doi.org/10.1016/j.emcon.2021.12.003.

Chen, G.Y., Zhou, T., Zhang, M., Ding, Z.X., Zhou, Z.K., Ji, Y.H., Tang, H.Y., Wang, C.S., 2023. Effects of heavy metal ions Cu^{2+}/Pb^{2+}/Zn^{2+} on kinetic rate constants of struvite crystallization. Chin. J. Chem. Eng. 57, 10–16. https://doi.org/10.1016/j.cjche.2022.06.032.

Chen, X.T., Li, Y.Y., Ma, Y.F., Li, B., Qin, Y.H., Li, X.M., Yuan, R., Chen, J.J., Huang, S.R., Li, H., Huang, H.M., 2026. Mitigation of adverse effects of calcium on struvite biomineralization for phosphorus recovery. Bioresour. Technol. 442, 133718. https://doi.org/10.1016/j.biortech.2025.133718.

Christl, I., Milne, C.J., Kinniburgh, D.G., Kretzschmar, R., 2001. Relating ion binding by fulvic and humic acids to chemical composition and molecular size. 2. metal binding. Environ. Sci. Technol. 35 (12), 2512–2517. https://doi.org/10.1021/es0002520.

Cordell, D., Drangert, J.O., White, S., 2009. The story of phosphorus: global food security and food for thought. Glob. Environ. Chang. 19 (2), 292–305. https://doi.org/10.1016/j.gloenvcha.2008.10.009.

Desmidt, E., Ghyselbrecht, K., Zhang, Y., Pinoy, L., Van der Bruggen, B., Verstraete, W., Rabaey, K., Meesschaert, B., 2015. Global phosphorus scarcity and full-scale p-recovery techniques: a review. Crit. Rev. Environ. Sci. Technol. 45 (4), 336–384. https://doi.org/10.1080/10643389.2013.866531.

Ditchfield, R., Hehre, W.J., Pople, J.A., 1971. Self-consistent molecular-orbital methods. ix. an extended gaussian-type basis for molecular-orbital studies of organic molecules. J. Chem. Phys. 54 (2), 724–728. https://doi.org/10.1063/1.1674902.

Do, Q.T., Nguyen, M.V., Doan, V.H., Chu, X.Q., Nguyen, Q.M., Thi, V.H.T., Kim, J.H., Lee, S., 2023. Heavy metals occurrence in the pig farm environment and the effects on an anaerobic digestion process of pig manure. Desalin. Water Treat. 296, 32–40. https://doi.org/10.5004/dwt.2023.29623.

Doyle, J.D., Parsons, S.A., 2002. Struvite formation, control and recovery. Water Res. 36 (16), 3925–3940. https://doi.org/10.1016/S0043-1354(02)00126-4.
Francl, M.M., Pietro, W.J., Hehre, W.J., Binkley, J.S., Gordon, M.S., DeFrees, D.J., Pople, J.A., 1982. Self-consistent molecular orbital methods. XXIII. a polarization-type basis set for second-row elements. J. Chem. Phys. 77 (7), 3654–3665. https://doi.org/10.1063/1.444267.
Frisch, M.J., 1992. Gaussian 92, Revision E. 3. Gaussian, Inc., Pittsburgh PA.
Gao, D.G., Huang, Y.F., Zhou, S.G., Li, B., Wang, G.Q., 2024a. Seawater boosts oxytetracycline (OTC) residues in struvite via hydroxyapatite (HAP) and dissolved organic matter (DOM) co-precipitation. J. Hazard. Mater. 480, 136355. https://doi.org/10.1016/j.jhazmat.2024.136355.
Gao, D.G., Li, B., Huang, X.W., Liu, X.N., Li, R.L., Ye, Z.L., Wu, X.F., Huang, Y.F., Wang, G.Q., 2023. A review of the migration mechanism of antibiotics during struvite recovery from wastewater. Chem. Eng. J. 466, 142983. https://doi.org/10.1016/j.cej.2023.142983.
Gao, D.G., Wu, X.F., Huang, Y.F., Zhou, S.G., Wang, G.Q., Li, B., 2024b. Deciphering the interplay between wastewater compositions and oxytetracycline in recovered struvite: Unveiling mechanisms and introducing control strategies. J. Hazard. Mater. 477, 135259. https://doi.org/10.1016/j.jhazmat.2024.135259.
Ge, X.F., Wang, L.J., Zhang, W.J., Putnis, C.V., 2020. Molecular understanding of humic acid-limited phosphate precipitation and transformation. Environ. Sci. Technol. 54 (1), 207–215. https://doi.org/10.1021/acs.est.9b05145.
Grimme, S., Antony, J., Ehrlich, S., Krieg, H., 2010. A consistent and accurate ab initio parametrization of density functional dispersion correction (DFT-D) for the 94 elements H-Pu. J. Chem. Phys. 132 (15), 154104. https://doi.org/10.1063/1.3382344.
Gu, C., Karthikeyan, K.G., 2005. Interaction of tetracycline with aluminum and iron hydrous oxides. Environ. Sci. Technol. 39 (8), 2660–2667. https://doi.org/10.1021/es048603o.
Hu, T.Y., He, P.J., Yang, Z., Wang, W., Zhang, H., Shao, L.M., Lu, F., 2022. Emission of airborne microplastics from municipal solid waste transfer stations in downtown. Sci. Total Environ. 828, 154400. https://doi.org/10.1016/j.scitotenv.2022.154400.
Huang, X.W., Ye, Z.L., Cai, J.S., Lin, L.F., 2021. Quantification of DOM effects on tetracyclines transport during struvite recovery from swine wastewater. Water Res. 206, 117756. https://doi.org/10.1016/j.watres.2021.117756.
Humphrey, W., Dalke, A., Schulten, K., 1996. VMD: Visual molecular dynamics. J. Mol. Graph. 14 (1), 33–38. https://doi.org/10.1016/0263-7855(96)00018-5.
Jin, X.B., Guo, J.Y., Hossain, M.F., Lu, J.J., Lu, Q.W., Zhou, Y., Zhou, Y.B., 2024. Recent advances in the removal and recovery of phosphorus from aqueous solution by metal-based adsorbents: a review. Resour. Conserv. Recycl. 204, 107464. https://doi.org/10.1016/j.resconrec.2024.107464.
Jupp, A.R., Beijer, S., Narain, G.C., Schipper, W., Slootweg, J.C., 2021. Phosphorus recovery and recycling - closing the loop. Chem. Soc. Rev. 50 (1), 87–101. https://doi.org/10.1039/d0cs01150a.
Kataki, S., West, H., Clarke, M., Baruah, D.C., 2016. Phosphorus recovery as struvite: recent concerns for use of seed, alternative Mg source, nitrogen conservation and fertilizer potential. Resour. Conserv. Recycl. 107, 142–156. https://doi.org/10.1016/j.resconrec.2015.12.009.
Le Corre, K.S., Valsami-Jones, E., Hobbs, P., Parsons, S.A., 2005. Impact of calcium on struvite crystal size, shape and purity. J. Cryst. Growth 283 (3–4), 514–522. https://doi.org/10.1016/j.jcrysgro.2005.06.012.
Le Corre, K.S., Valsami-Jones, E., Hobbs, P., Parsons, S.A., 2007. Kinetics of struvite precipitation: effect of the magnesium dose on induction times and precipitation rates. Environ. Technol. 28 (12), 1317–1324. https://doi.org/10.1080/09593332808618891.
Le Corre, K.S., Valsami-Jones, E., Hobbs, P., Parsons, S.A., 2009. Phosphorus recovery from wastewater by struvite crystallization: a review. Crit. Rev. Environ. Sci. Technol. 39 (6), 433–477. https://doi.org/10.1080/10643380701640573.
Li, B., Boiarkina, I., Yu, W., Huang, H.M., Munir, T., Wang, G.Q., Young, B.R., 2019. Phosphorous recovery through struvite crystallization: challenges for future design. Sci. Total Environ. 648, 1244–1256. https://doi.org/10.1016/j.scitotenv.2018.07.166.
Li, F.H., Wu, W.H., Li, R.Y., Fu, X.R., 2016. Adsorption of phosphate by acid-modified fly ash and palygorskite in aqueous solution: experimental and modeling. Appl. Clay Sci. 132, 343–352. https://doi.org/10.1016/j.clay.2016.06.028.
Liao, W.Q., Huang, X.W., Ye, Z.L., Zhang, T.Y., Cai, J.S., Huang, Y.H., Li, Y.L., 2025. Insights into the migration mechanism of extracellular antibiotic resistance genes during struvite recovery using synthetic wastewater. Water Res. 268, 122681. https://doi.org/10.1016/j.watres.2024.122681.
Liu, X.N., Wang, J., 2019. Impact of calcium on struvite crystallization in the wastewater and its competition with magnesium. Chem. Eng. J. 378, 122121. https://doi.org/10.1016/j.cej.2019.122121.
Liu, X.N., Wen, G.Q., Hu, Z.Y., Wang, J., 2018. Coupling effects of pH and Mg/P ratio on P recovery from anaerobic digester supernatant by struvite formation. J. Clean. Prod. 198, 633–641. https://doi.org/10.1016/j.jclepro.2018.07.073.
Lou, Y.Y., Ye, Z.L., Chen, S.H., Wei, Q.S., Zhang, J.Q., Ye, X., 2018. Influences of dissolved organic matters on tetracyclines transport in the process of struvite recovery from swine wastewater. Water Res. 134, 311–326. https://doi.org/10.1016/j.watres.2018.02.010.
Lu, T., 2024. A comprehensive electron wavefunction analysis toolbox for chemists. Multiwfn. J. Chem. Phys. 161 (8), 082503. https://doi.org/10.1063/5.0216272.
Lu, T., Chen, F.W., 2012. Multiwfn: a multifunctional wavefunction analyzer. J. Comput. Chem. 33 (5), 580–592. https://doi.org/10.1002/jcc.22885.
Lu, T., Chen, Q.X., 2021. Interaction region indicator: a simple real space function clearly revealing both chemical bonds and weak interactions. Chemistry-Methods 1 (5), 231–239. https://doi.org/10.1002/cmtd.202100007.
Ma, M.Y., Han, R.X., Han, R.Q., Xu, D.F., Li, F.H., 2024. Binding between Cu^{2+}/Zn^{2+} and aged polyethylene and polyethylene terephthalate microplastics in swine wastewaters: Adsorption behavior, and mechanism insights. Environ. Pollut. 360, 124685. https://doi.org/10.1016/j.envpol.2024.124685.
Marenich, A.V., Cramer, C.J., Truhlar, D.G., 2009. Universal solvation model based on solute electron density and on a continuum model of the solvent defined by the bulk dielectric constant and atomic surface tensions. J. Phys. Chem. B 113 (18), 6378–6396. https://doi.org/10.1021/jp810292n.
Mehta, C.M., Batstone, D.J., 2013. Nucleation and growth kinetics of struvite crystallization. Water Res. 47 (8), 2890–2900. https://doi.org/10.1016/j.watres.2013.03.007.
Nelson, N.O., Mikkelsen, R.L., Hesterberg, D.L., 2003. Struvite precipitation in anaerobic swine lagoon liquid: effect of pH and Mg : P ratio and determination of rate constant. Bioresour. Technol. 89 (3), 229–236. https://doi.org/10.1016/S0960-8524(03)00076-2.
Perwitasari, D.S., Muryanto, S., Jamari, J., Bayuseno, A.P., 2018. Kinetics and morphology analysis of struvite precipitated from aqueous solution under the influence of heavy metals: Cu^{2+}, Pb^{2+}, Zn^{2+}. J. Environ. Chem. Eng. 6 (1), 37–43. https://doi.org/10.1016/j.jece.2017.11.052.
Rabinovich, A., Rouff, A.A., 2023. Changes to struvite growth and morphology as impacted by low molecular weight organics. ACS ES&T Water 3 (8), 2277–2285. https://doi.org/10.1021/acsestwater.3c00062.
Rouff, A.A., Ramlogan, M.V., Rabinovich, A., 2016. Synergistic removal of zinc and copper in greenhouse waste effluent by struvite. ACS Sustain. Chem. Eng. 4 (3), 1319–1327. https://doi.org/10.1021/acssuschemeng.5b01348.
Shih, Y.J., Abarca, R.R.M., de Luna, M.D.G., Huang, Y.H., Lu, M.C., 2017. Recovery of phosphorus from synthetic wastewaters by struvite crystallization in a fluidized-bed reactor: effects of pH, phosphate concentration and coexisting ions. Chemosphere 173, 466–473. https://doi.org/10.1016/j.chemosphere.2017.01.088.
Shim, S., Won, S., Reza, A., Kim, S., Ahmed, N., Ra, C., 2020. Design and optimization of fluidized bed reactor operating conditions for struvite recovery process from swine wastewater. Processes 8 (4), 422. https://doi.org/10.3390/pr8040422.
Stephens, P.J., Devlin, F.J., Chabalowski, C.F., Frisch, M.J., 1994. Ab-Initio calculation of vibrational absorption and circular-dichroism spectra using density-functional force-fields. J. Phys. Chem. 98 (45), 11623–11627. https://doi.org/10.1021/j100096a001.
Tang, C., Liu, Z., Peng, C., Chai, L.-Y., Kuroda, K., Okido, M., Song, Y.-X., 2019. New insights into the interaction between heavy metals and struvite: struvite as platform for heterogeneous nucleation of heavy metal hydroxide. Chem. Eng. J. 365, 60–69. https://doi.org/10.1016/j.cej.2019.02.034.
Wang, H., Tian, Z.Y., Wang, H., Yan, Q., 2020a. Optimization and reaction kinetics analysis for phosphorus removal in struvite precipitation process. Water Environ. Res 92 (8), 1162–1172. https://doi.org/10.1002/wer.1311.
Wang, Q.J., Zhang, Y., Wangjin, X.X., Wang, Y.L., Meng, G.H., Chen, Y.H., 2020b. The adsorption behavior of metals in aqueous solution by microplastics effected by UV radiation. J. Environ. Sci.- China 87, 272–280. https://doi.org/10.1016/j.jes.2019.07.006.
Wang, S.N., Yuan, Y., Bi, E.R., 2024. The role of magnesium ion in the interactions between humic acid and tetracycline in solution. J. Environ. Manage. 354, 120344. https://doi.org/10.1016/j.jenvman.2024.120344.
Wang, Y., Wang, X.J., Li, J., Li, Y., Liu, Y.Y., Wang, F., Zhao, J.F., 2020c. Adsorption and precipitation behaviors of zinc, copper and tetracycline with struvite products obtained by phosphorus recovery from swine wastewater. J. Environ. Chem. Eng. 8 (6), 104488. https://doi.org/10.1016/j.jece.2020.104488.
Wang, Y., Wang, X.J., Li, Y., Li, J., Liu, Y.Y., Xia, S.Q., Zhao, J.F., 2021. Effects of exposure of polyethylene microplastics to air, water and soil on their adsorption behaviors for copper and tetracycline. Chem. Eng. J. 404, 126412. https://doi.org/10.1016/j.cej.2020.126412.
Weigend, F., Ahlrichs, R., 2005. Balanced basis sets of split valence, triple zeta valence and quadruple zeta valence quality for H to Rn: design and assessment of accuracy. PCCP 7 (18), 3297–3305. https://doi.org/10.1039/b508541a.
Wu, J.Z., Li, Y.F., Xu, B.J., Li, M., Wang, J., Shao, Y.N., Chen, F.Y., Sun, M., Liu, B., 2022. Effects of physicochemical parameters on struvite crystallization based on kinetics. Int. J. Environ. Res. Public Health 19 (12), 7204. https://doi.org/10.3390/ijerph19127204.
Wu, R.T., Cai, Y.F., Chen, Y.X., Yang, Y.W., Xing, S.C., Liao, X.D., 2021. Occurrence of microplastic in livestock and poultry manure in South China. Environ. Pollut. 277, 116790. https://doi.org/10.1016/j.envpol.2021.116790.
Yan, H.L., Shih, K., 2016. Effects of calcium and ferric ions on struvite precipitation: a new assessment based on quantitative X-ray diffraction analysis. Water Res. 95, 310–318. https://doi.org/10.1016/j.watres.2016.03.032.
Yan, J.N., Ma, M.Y., Li, F.H., 2024. Phosphorus recovery via struvite crystallization in batch and fluidized-bed reactors: Roles of microplastics and dissolved organic matter. J. Hazard. Mater. 476, 135108. https://doi.org/10.1016/j.jhazmat.2024.135108.
Yang, S., Hu, A.D., Zhang, J., Yu, W., Wu, X.F., Huang, Y.F., Zhou, S.G., Li, B., Wang, G.Q., 2025. Light-driven biohybrid for phosphorus recovery via struvite biomineralization in tetracycline-laden livestock wastewater. Water Res. 282, 123745. https://doi.org/10.1016/j.watres.2025.123745.
Zahid, M.B., Wang, X.F., Xia, Y.F., Xu, X.Y., Li, D.W., Li, F.H., 2025. Roles of dissolved organic matters in K-struvite formation in batch and fluidized-bed reactors: a kinetic

insight. J. Environ. Chem. Eng. 13 (5), 118515. https://doi.org/10.1016/j.jece.2025.118515.
Zhang, Q., Zhao, S.P., Ye, X.Z., Xiao, W.D., 2016. Effects of organic substances on struvite crystallization and recovery. Desalin. Water Treat. 57 (23), 10924–10933. https://doi.org/10.1080/19443994.2015.1040850.
Zhao, Y., Truhlar, D.G., 2008. The M06 suite of density functionals for main group thermochemistry, thermochemical kinetics, noncovalent interactions, excited states, and transition elements: two new functionals and systematic testing of four M06-class functionals and 12 other functionals. Theor. Chem. Acc. 120 (1–3), 215–241. https://doi.org/10.1007/s00214-007-0310-x.